10522 *Inorg. Chem.* **2010**, *49*, 10522–10535
DOI: 10.1021/ic101541q

Inorganic Chemistry
Article

Eu^{3+}/Tb^{3+}-Doped $La_2O_2CO_3/La_2O_3$ Nano/Microcrystals with Multiform Morphologies: Facile Synthesis, Growth Mechanism, and Luminescence Properties

Guogang Li, Chong Peng, Cuimiao Zhang, Zhenhe Xu, Mengmeng Shang, Dongmei Yang, Xiaojiao Kang, Wenxin Wang, Chunxia Li, Ziyong Cheng, and Jun Lin*

State Key Laboratory of Rare Earth Resources Utilization, Changchun Institute of Applied Chemistry, Chinese Academy of Sciences, Changchun 130022, People's Republic of China, and Graduate University of the Chinese Academy of Sciences, Beijing 100049, People's Republic of China

Received July 31, 2010

$LaCO_3OH$ nano/microcrystals with a variety of morphologies/sizes including nanoflakes, microflowers, nano/microrhombuses, two-double microhexagrams sandwichlike microspindles, and peach-nucleus-shaped microcrystals have been synthesized via a facile homogeneous precipitation route under mild conditions. A series of controlled experiments indicate that the pH values in the initial reaction systems, carbon sources, and simple ions (NH_4^+ and Na^+) were responsible for the shape determination of the $LaCO_3OH$ products. A possible formation mechanism for these products with diverse architectures has been presented. After annealing at suitable temperatures, $LaCO_3OH$ was easily converted to $La_2O_2CO_3$ and La_2O_3 with the initial morphologies. A systematic study on the photoluminescence and cathodoluminescence properties of Eu^{3+}- or Tb^{3+}-doped $La_2O_2CO_3/La_2O_3$ samples has been performed in detail. The excitation and site-selective emission spectra were recorded to investigate the microstructure, site symmetry, and difference in the $^5D_0 \rightarrow {}^7F_2$ transition of Eu^{3+} ions in $La_2O_2CO_3$ and La_2O_3 host lattices. In addition, the dependence of the luminescent intensity on the morphology for the as-prepared $La_2O_2CO_3/La_2O_3:Ln^{3+}$ (Ln = Eu, Tb) samples has been investigated. The ability of generating diverse morphologies and multiemitting colors for different rare-earth activator ion (Ln = Eu, Tb) doped $La_2O_2CO_3/La_2O_3$ nano/microstructures provides a great opportunity for the systematic evaluation of morphology-dependent luminescence properties, as well as the full exploration of their application in many types of color display fields.

1. Introduction

Recently, the synthesis of inorganic nano/microstructures with novel and controllable morphologies has stimulated considerable attention in the whole chemical and material science world, because it is well-known that the chemical and physical properties of the materials closely interrelate with geometrical factors such as morphology, size, dimensionality as well as composition, crystal type, and phase. Accordingly, rational control over these factors allows us not only to observe unique properties of the materials but also to tune their chemical and physical properties as desired, which has potential application in many fields, including catalysis,[1] optics,[2] biological labeling,[3] magnetism,[4] nanoelectronics and optoelectronic devices, etc.[5] To date, many efforts have been made to explore excellent approaches to the fabrication of shape-controllable inorganic crystals to enhance their performance in currently existing applications. Among them, the wet chemical route has been proved to be one of the most effective and convenient approaches in preparing various inorganic materials with diversely controllable morphologies and architectures in terms of cost and potential for large-scale production.[6] Generally, it can be classified as two kinds: the first one is the template method, which employs either hard templates such as polymeric core supports and sacrificial metal substrates or soft templates such as micelles in emulsions or ionic liquids.[7] The other one is the template-free

---

*To whom correspondence should be addressed. E-mail: jlin@ciac.jl.cn.

[1] Sun, C. W.; Sun, J.; Xiao, G. L.; Zhang, H. R.; Qiu, X. P.; Li, H.; Chen, L. Q. *J. Phys. Chem. B* **2006**, *110*, 13445.

[2] (a) Mai, H. X.; Zhang, Y. W.; Si, R.; Yan, Z. G.; Sun, L. D.; You, L. P.; Yan, C. H. *J. Am. Chem. Soc.* **2006**, *128*, 6426. (b) Wang, X.; Zhuang, J.; Peng, Q.; Li, Y. D. *Inorg. Chem.* **2006**, *45*, 6661.

[3] Yi, G. S.; Lu, H. C.; Zhao, S. Y.; Ge, Y.; Yang, W. J.; Chen, D. P.; Guo, L. H. *Nano Lett.* **2002**, *2*, 733.

[4] Lu, H. C.; Yi, G. S.; Zhao, S. Y.; Chen, D. P.; Guo, L. H.; Cheng, J. *J. Mater. Chem.* **2004**, *14*, 1336.

[5] (a) Im, S. H.; Lee, Y. T.; Wiely, B.; Xia, Y. N. *Angew. Chem., Int. Ed.* **2005**, *44*, 2154. (b) Cheng, F. C.; Zhao, J. Z.; Li, C. S.; Ma, H.; Chen, J.; Shen, P. W. *Inorg. Chem.* **2006**, *45*, 2038.

[6] Lin, J.; Yu, M.; Lin, C. K.; Liu, X. M. *J. Phys. Chem. C* **2007**, *111*, 5835.

[7] (a) Han, W.; Fan, S.; Li, Q.; Hu, Y. *Science* **1997**, *277*, 1287. (b) Yada, M.; Mihara, M.; Mouri, S.; Kuroki, M.; Kijima, T. *Adv. Mater.* **2002**, *14*, 309. (c) Sun, X. M.; Li, Y. D. *Angew. Chem., Int. Ed.* **2004**, *43*, 3827. (d) Jacob, D. S.; Bitton, L.; Grinblat, J.; Felner, I.; Koltypin, Y.; Gedanken, A. *Chem. Mater.* **2006**, *18*, 3162.

method, which is facile and efficient compared with the template method.[8] The addition of a template to the reaction system involves a complicated process and may brighten in impurities because of the incomplete removal of the template. Therefore, the latter method seems to be more attractive and promising because of its higher yield and simplicity.

Field-emission displays (FEDs) are considered to be the most promising next-generation flat-panel display technique because of their potential to provide display with a thin panel, self-emission, wide viewing, quick response time, high brightness, high contrast ratio, light weight, and low-power consumption.[9] In order to realize the full-color FEDs, one of the most important factors is to develop highly efficient trichromatic low-voltage phosphors. Rare-earth (RE) ion-doped luminescent materials display interesting optical characteristics and abundant emission colors, which are poised to be exploited in the development of displays and phosphor applications. This is largely because of their unique intra 4f transitions, which are less influenced by the ligand field (because of shielding of the 4f orbitals by the outer 5s and 5p orbitals), leading to sharp emissions.[10] For example, the trivalent europium (Eu^{3+}) ion is well-known as a red-emitting activator because of its $^5D_0 \rightarrow {}^7F_J$ ($J = 0, 1, 2, 3, 4$) transitions and the trivalent terbium (Tb^{3+}) ion is commonly employed as a green activator because of the efficient emission originating from the $^5D_4 \rightarrow {}^7F_J$ ($J = 6, 5, 4, 3$) transitions.[11] Except for activators, suitable host materials for RE ion doping are also important for the preparation of highly efficient phosphors. Among various RE^{3+}-activated luminescent materials, yttrium-based lattices, such as Y_2O_3,[12] YBO_3,[13] YVO_4,[14] among others, are usually used as hosts because of their suitable crystal structure and high chemical stability. In comparison with Y, La is more abundant in RE mineral resources and La_2O_3 is much cheaper than Y_2O_3. However, the development of La-based materials is still inadequate, and La_2O_3 is overstocked in the RE industry. It is valuable to fundamentally and practically study the La-based materials for the balanced utilization of the RE natural resources. Furthermore, inorganic compounds containing lanthanum are recognized as excellent host materials for RE activators because RE doping levels can be controlled over a wide range without changing host crystal structures. RE ions can be homogeneously substituted for La^{3+} ions, which results in good luminescent properties. As such, La_2O_3:Eu^{3+} have been investigated as red phosphors.[15] Besides lanthanum oxides, lanthanum oxycarbonates with hexagonal type II structure are also suitable for the host materials of phosphors[16,17] because they have a high chemical stability against both water and carbon dioxide, and the structure of type II oxycarbonates is similar to conventional A-type lanthanum sesquioxides. However, it is difficult to obtain type II oxycarbonates in a single phase using conventional methods because tetragonal type I or monoclinic type Ia oxycarbonates are formed via the thermal decomposition of acetates, carbonates, and oxalates, or it is necessary to heat the oxide at 773 K at least for 1 week under a humid CO_2 atmosphere to obtain type II oxycarbonates.[17] Therefore, exploring facile and efficient methods to prepare RE ion-doped lanthanum oxides and oxycarbonates is helpful for their applications in displays and phosphors. On the other hand, among compounds of the RE family, lanthanum compounds with various morphologies have been synthesized, such as nanorods, macropores, nanowires, and nanoplates of La_2O_3,[18] nanospheres, nanowires, and nanorods of $La(OH)_3$,[18a,19] needlelike and spherical $La_2(CO_3)_3$,[20] nanowires of $LaPO_4$,[21] triangular nanoplates and flakes of LaF_3,[22] etc., but rare-earth hydroxycarbonates with novel morphologies have rarely been investigated especially for lanthanum hydroxycarbonates.[23]

Herein, we employed a facile and efficient homogeneous precipitation method to successfully prepare lanthanum hydroxycarbonates ($LaCO_3OH$) at mild conditions. Moreover, by simple changes of the carbon sources [$CO(NH_2)_2$, Na_2CO_3, $NaHCO_3$, $(NH_4)_2CO_3$, and NH_4HCO_3] and pH values of the initial solution, multiform $LaCO_3OH$ products such as flakes, flowers, rhombuses, two-double hexagrams, sandwichlike spindles, peach-nucleus-shaped crystals, and so on were obtained. The effects of the solution pH and carbon sources on the crystal phase, size, and morphology of the $LaCO_3OH$ products were studied in detail, and a formation

---

(8) Liu, J. P.; Huang, X. T.; Li, Y. Y.; Sulieman, K. M.; He, X.; Sun, F. L. *Cryst. Growth Des.* **2006**, *6*, 1690.

(9) (a) Jüstel, T.; Nikol, H.; Ronda, C. *Angew. Chem., Int. Ed.* **1998**, *37*, 3084. (b) Hirosaki, N.; Xie, R.; Inoue, K.; Sekiguchi, T.; Dierre, B.; Tamura, K. *Appl. Phys. Lett.* **2007**, *91*, 061101. (c) Jiang, Y. D.; Zhang, F.; Summers, C. J.; Wang, Z. L. *Appl. Phys. Lett.* **1999**, *74*, 1677.

(10) Blasse, G.; Grabmaier, B. C. *Luminescence Materials*; Springer-Verlag: Berlin, 1994; Chapters 4 and 5.

(11) (a) Liu, X. M.; Lin, C. K.; Lin, J. *Appl. Phys. Lett.* **2007**, *90*, 081904. (b) Liu, X. M.; Lin, J. *J. Mater. Chem.* **2008**, *18*, 221. (c) Sohn, K. S.; Choi, Y. G.; Choi, Y. Y.; Park, H. D. *J. Electrochem. Soc.* **2000**, *147*, 3552. (d) Sohn, K. S.; Shin, N. *Electrochem. Solid-State Lett.* **2002**, *5*, H21. (e) Che, P.; Meng, J.; Guo, L. *J. Lumin.* **2007**, *122*, 168.

(12) (a) Oka, Y.; Yao, T.; Yamamoto, N. *J. Solid State Chem.* **2000**, *152*, 486. (b) Yang, J.; Quan, Z. W.; Kong, D. Y.; Liu, X. M.; Lin, J. *Cryst. Growth Des.* **2007**, *7*, 731. (c) Chi, L. S.; Liu, R. S.; Lee, B. J. *J. Electrochem. Soc.* **2005**, *152*, J93.

(13) (a) Jia, C. J.; Sun, L. D.; You, L. P.; Jiang, X. C.; Luo, F.; Pang, Y. C.; Yan, C. H. *J. Phys. Chem. B* **2005**, *109*, 3284. (b) Lin, C. K.; Kong, D. Y.; Liu, X. M.; Wang, H.; Yu, M.; Lin, J. *Inorg. Chem.* **2007**, *46*, 2674. (c) Xu, Z. H.; Li, C. X.; Cheng, Z. Y.; Zhang, C. M.; Li, G. G.; Peng, C.; Lin, J. *CrystEngComm* **2010**, *12*, 549.

(14) (a) Jia, C. J.; Sun, L. D.; Luo, F.; Jiang, X. C.; Wei, L. H.; Yan, C. H. *Appl. Phys. Lett.* **2004**, *84*, 5305. (b) Hou, Z. Y.; Yang, P. P.; Li, C. X.; Wang, L. L.; Lian, H. Z.; Quan, Z. W.; Lin, J. *Chem. Mater.* **2008**, *20*, 6686. (c) Yu, M.; Lin, J.; Wang, Z.; Fu, J.; Wang, S.; Zhang, H. J.; Han, Y. C. *Chem. Mater.* **2002**, *14*, 2224. (d) Yu, M.; Lin, J.; Fang, J. *Chem. Mater.* **2005**, *17*, 1783.

(15) (a) Chang, J. J.; Xiong, S.; Peng, H. S.; Sun, L. D.; Lu, S. Z.; You, F. T.; Huang, S. H. *J. Lumin.* **2007**, *122*, 844. (b) Liu, H. Q.; Wang, L. L.; Chen, S. Q.; Zou, B. S. *J. Lumin.* **2007**, *126*, 459. (c) Hosono, E.; Fujihara, S. *Chem. Commun.* **2004**, 2062.

(16) (a) Masui, T.; Koyabu, K.; Tamura, S.; Imanaka, N. *J. Mater. Sci.* **2005**, *40*, 4121. (b) Koyabu, K.; Masui, T.; Tamura, S.; Imanaka, N. *J. Alloys Compd.* **2006**, *408*, 867. (c) Mayama, Y.; Koyabu, K.; Masui, T.; Tamura, S.; Imanaka, N. *J. Alloys Compd.* **2006**, *418*, 243. (d) Niu, H. L.; Min, Q.; Tao, Z. Y.; Song, J. M.; Mao, C. J.; Zhang, S. Y.; Chen, Q. W. DOI:10.1016/j.jallcom.2010.09.056

(17) (a) Höläs, J.; Turkki, T. *Thermochim. Acta* **1991**, *190*, 335. (b) Moune-Minn, O. K.; Caro, P. *J. Crystallogr. Spectrosc. Res.* **1982**, *12*, 157.

(18) (a) Wu, Q. Z.; Shen, Y.; Liao, J. F.; Li, Y. G. *Mater. Lett.* **2004**, *58*, 2688. (b) Tang, B.; Ge, J. C.; Wu, C. J.; Zhuo, L. H.; Niu, J. Y.; Chen, Z. Z.; Shi, Z. Q.; Dong, Y. B. *Nanotechnology* **2004**, *15*, 1273. (c) Mu, Q. Y.; Wang, Y. D DOI:10.1016/j.jallcom.2010.09.041

(19) Wang, X.; Li, Y. D. *Angew. Chem., Int. Ed.* **2002**, *41*, 4790.

(20) Jeevanandam, P.; Koltypin, Y.; Palchik, O.; Gedanken, A. *J. Mater. Chem.* **2001**, *11*, 869.

(21) (a) Fang, Y. P.; Xu, A. W.; Song, R. Q.; Zhang, H. X.; You, L. P.; Yu, J. C.; Liu, H. Q. *J. Am. Chem. Soc.* **2003**, *125*, 16025. (b) Zhang, Y. J.; Guan, H. M. *Mater. Res. Bull.* **2005**, *40*, 1536.

(22) Zhang, Y. W.; Sun, X.; Si, R.; You, L. P.; Yan, C. H. *J. Am. Chem. Soc.* **2005**, *127*, 3260.

(23) (a) Sun, C. W.; Xiao, G. L.; Li, H.; Chen, L. Q. *J. Am. Ceram. Soc.* **2007**, *90*, 2576. (b) Pol, V. G.; Thiyagarajan, P.; Calderon Moreno, J. M.; Popa, M. *Inorg. Chem.* **2009**, *48*, 6417. (c) Zhang, Y. J.; Han, K. D.; Cheng, T.; Fang, Z. Y. *Inorg. Chem.* **2007**, *46*, 4713. (d) Xie, J. S.; Wu, Q. S.; Zhang, D.; Ding, Y. P. *Cryst. Growth Des.* **2009**, *9*, 3889.

mechanism was proposed. After annealing of the as-prepared $LaCO_3OH$ products at different temperatures (600 and 800 °C, respectively) for only several hours, the $La_2O_2CO_3$ and La_2O_3 products were obtained with maintained morphologies. More importantly, we concentrated on the photoluminescence (PL) and cathodoluminescence (CL) properties of $La_2O_2CO_3/La_2O_3:Eu^{3+}$ or Tb^{3+} phosphors in an effort to adjust the emission colors of the final products. The excitation and site-selective emission spectroscopy were applied to investigate the microstructure, site symmetry, and difference in the $^5D_0 \rightarrow {}^7F_2$ transition of Eu^{3+} ions in $La_2O_2CO_3$ and La_2O_3 host lattices. In addition, we also investigated the effect of the morphologies of $La_2O_2CO_3/La_2O_3:Eu^{3+}$ or Tb^{3+} phosphors on their luminescence properties.

2. Experimental Section

Chemicals and Materials. The initial rare-earth oxides, including La_2O_3 (99.999%), Eu_2O_3 (99.999%), and Tb_4O_7 (99.999%), were purchased from Science and Technology Parent Company of Changchun Institute of Applied Chemistry, and other chemicals including HNO_3 (65–68 wt %), $NH_3 \cdot H_2O$ (25 wt %), $CO(NH_2)_2$, Na_2CO_3, $NaHCO_3$, $(NH_4)_2CO_3$, and NH_4HCO_3 (analytical grade) were purchased from Beijing Chemical Company. All chemicals were of analytical-grade reagents and were used directly without further purification.

Preparation of $LaCO_3OH$. A lanthanum nitrate stock solution of 0.5 M was prepared by dissolving the corresponding metal oxide in nitric acid at elevated temperature. In a typical procedure, 15 mL of $La(NO_3)_3$ (0.5 M) was added into a 300 mL of aqueous solution. After vigorous stirring for 10 min, 0.25 mol of $CO(NH_3)_2$ was added into the above solution and then distilled water was added to make a total volume of 500 mL. The pH of the mixture was subsequently adjusted to 2 by adding HNO_3 (1 M), and the beaker was wrapped with a polyethylene film. After additional agitation for 30 min, the mixed solution was heated on a hot plate with strong stirring to 90 °C within 60 min and then maintained at 90 °C for 2 h. The suspension was naturally cooled to room temperature, and the resulting precipitates were separated by centrifugation, respectively washed with deionized water and anhydrous ethanol in sequence four times, and then dried at 80 °C in air for 12 h. The as-prepared product was denoted as **P1**. Other samples (**P2**–**P15**) were prepared by a similar procedure except for different carbon sources and pH conditions. The pH of the mixture was adjusted to a specific value by adding $NH_3 \cdot H_2O$ (25 wt %) or a HNO_3 (1 M) solution. The detailed experimental parameters are summarized in Table 1 in the Supporting Information. It should be stated that all samples reacted through a homogeneous precipitation process at 90 °C for 2 h.

Preparation of $LaCO_3OH:Ln^{3+}$ and $La_2O_2CO_3/La_2O_3:Ln^{3+}$ (Ln = Eu, Tb). First, La_2O_3, Eu_2O_3, and Tb_4O_7 were dissolved in dilute HNO_3, respectively, resulting in the formation of a colorless stock solution of $La(NO_3)_3$ (0.5 M) and $Ln(NO_3)_3$ (Ln = Eu, Tb; 0.2 M). In a typical synthesis, stoichiometric $La(NO_3)_3$ and $Ln(NO_3)_3$ (solution) were dissolved in deionized water, resulting in the formation of a colorless solution of $La(NO_3)_3$ and $Ln(NO_3)_3$ (Ln = Eu, Tb); $Ln^{3+}/(La^{3+} + Ln^{3+})$ = 0.1–10 mol %. Then $LaCO_3OH:Ln^{3+}$ products can be obtained through the same preparation process of the $LaCO_3OH$ products as stated above. The final $La_2O_2CO_3:Ln^{3+}$ and $La_2O_3:Ln^{3+}$ (Ln = Eu, Tb) products were retrieved through a heat treatment of the $LaCO_3OH:Ln^{3+}$ products at 600 and 800 °C in air for 4 h, respectively.

Characterization. Power X-ray diffraction (XRD) measurements were performed on a D8 Focus diffractometer at a scanning rate of 10° min^{-1} in the 2θ range from 10° to 80°, with graphite-monochromatized Cu Kα radiation (λ = 0.154 05 nm). Fourier transform infrared spectroscopy (FT-IR) spectra were performed on a Perkin-Elmer 580B IR spectrophotometer using the KBr pellet technique. Thermogravimetric and differential thermal analysis (TG-DTA) data were recorded with a thermal analysis instrument (SDT 2960, TA Instruments, New Castle, DE) with a heating rate of 10 °C min^{-1} in an air flow of 100 mL min^{-1}. The morphology and composition of the samples were inspected using a field-emission scanning electron microscope (S-4800, Hitachi) equipped with an energy-dispersive X-ray (EDX) spectrometer. Low- to high-resolution transmission electron microscopy (TEM) and selected area electron diffraction (SAED) patterns were recorded using a FEI Tecnai G2 S-Twin with a field-emission gun operating at 200 kV. Images were acquired digitally on a Gatan multipole CCD camera. PL excitation and emission spectra were recorded with a Hitachi F-4500 spectrophotometer equipped with a 150 W xenon lamp as the excitation source. For the excitation and site-selective emission measurements, the excitation source was a dye laser (Spectron Laser Systems SL4000) pumped by the second harmonic (532 nm) of a pulsed Nd:yttrium aluminum garnet laser (Spectron Laser Systems SL802G). The laser beam was focused on the sample with a cross-sectional area of about 3 mm^2. The pulse energy was about 5 mJ with a 10 Hz repetition rate and a 5 ns duration. The sample was placed in a helium-gas-flow cryostat for measurements in the variable-temperature region (10–305 K). The luminescence was dispersed by a 75 cm monochromator (Acton Research Corp. Pro-750) and observed with a photomultiplier tube (Hamamatsu R928). Suitable filters were used to eliminate the intense laser scattering. The excitation spectra of the $^7F_0 \rightarrow {}^5D_0$ transition were obtained by monitoring the total luminescence by setting the monochromator in zero order of diffraction to pass all of the $^5D_0 \rightarrow {}^7F_J$ (J = 1, 2, ..., 6) emission in which a 580 nm cutoff filter was used. Time-integrated signals from a digital storage oscilloscope (LeCroy 9310A) were recorded for the emission and excitation spectra under pulsed laser excitation. CL measurements were carried out in an ultrahigh-vacuum chamber ($< 10^{-8}$ Torr), where the phosphors were excited by an electron beam in the voltage range of 0.5–5.0 kV and different filament currents, and the emission spectra were recorded using an F-4500 spectrophotometer. The PL quantum yield (QY) was measured by an absolute PL QY measurement system C9920-02. All of the measurements were performed at room temperature.

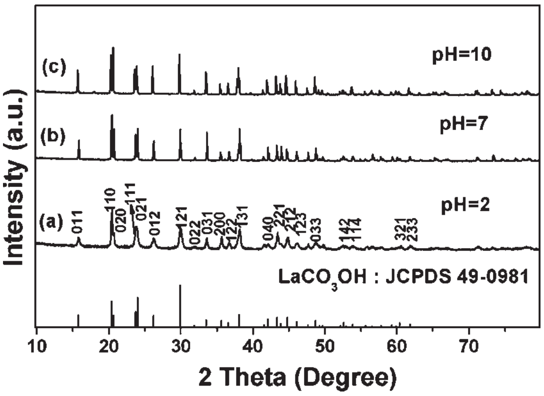

Figure 1. XRD patterns of the as-prepared $LaCO_3OH$ products using $CO(NH_3)_2$ as the carbon source at different pH values of (a) 2, (b) 7, and (c) 10 at 90 °C for 2 h. The standard data of orthorhombic $LaCO_3OH$ (JCPDS no. 49-0981) were used as references.

3. Results and Discussion

3.1. Structure, Morphology, and Growth Mechanism of $LaCO_3OH$.

Structure. The composition and phase purity of the products were first examined by XRD. Figure 1 shows the XRD patterns of the La_2CO_3OH products prepared by using $CO(NH_3)_2$ as the carbon source with a

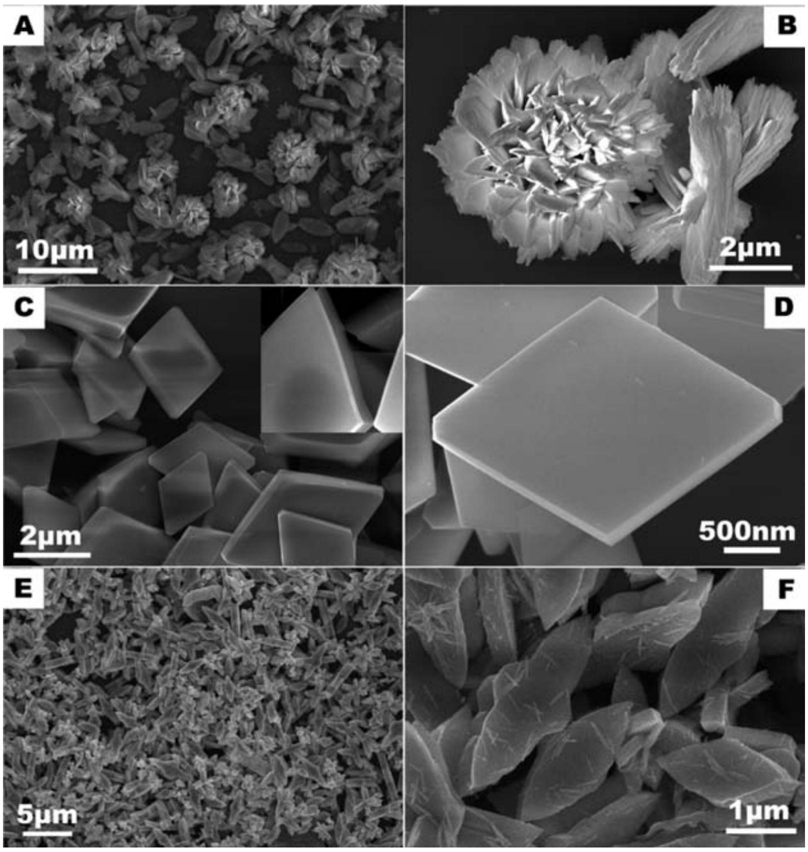

Figure 2. Influence of the pH values on the shapes of the nano/microcrystals with $CO(NH_3)_2$ as the carbon source: (A and B) elliptical nanoflakes and microflowers obtained at pH = 2; (C and D) rhombic microplates obtained at pH = 7; (E and F) sandwichlike microspindles obtained at pH = 10.

homogeneous precipitation process at 90 °C for 2 h under various pH conditions of (a) pH = 2, (b) pH = 7, and (c) pH = 10. On the basis of the Joint Committee on Power Diffraction Standard (JCPDS) reference database, the diffraction peaks of the three samples can be assigned to a pure orthorhombic $LaCO_3OH$ phase, which coincides well with the literature values (JCPDS no.49-0981). No peak shifts and other impurity phases appear in this figure, indicating the high purity and crystallinity of the products. It is worth pointing out that the XRD patterns of the three samples also show that there are large differences in the relative intensities based on (110), (021), (012), and (121) peaks compared with the standard data, indicating the possibility of different preferential orientation growth under different pH values. Except for the use of $CO(NH_3)_2$ as the carbon source, we also investigate the effects of $NaHCO_3$, NH_4HCO_3, Na_2CO_3, and $(NH_4)_2CO_3$ used as carbon sources on the crystal structures and morphologies of the products. The cases of using $NaHCO_3$, NH_4HCO_3, Na_2CO_3, and $(NH_4)_2CO_3$ as carbon sources are similar to that of using $CO(NH_3)_2$ as the carbon source. The XRD peaks of **P4**−**P11** samples all can be indexed as a pure orthorhombic $LaCO_3OH$ phase, indicating that the different carbon sources do not change the crystal phases of the products. However, when **P4** is compared with **P6**, **P8**, and **P10** samples, the differences in the relative intensities based on (011), (110), (020), (111), (021), (012), and (121) peaks indicate different preferential orientation growth under the different carbon sources, as shown in Figure S1 (Supporting Information). In general, the above results suggest that different products have different growth habits under diverse reaction conditions.

To further validate the formation of $LaCO_3OH$ products, we measured the FT-IR of the as-prepared products by using the **P2** sample as a representative example, as shown in Figure S2 (Supporting Information). The absorptions between 3300 and 3700 cm^{-1} with peaks at 3540 and 3433 cm^{-1} are due to the stretching mode of OH, ν_{OH}, which are assigned to structural OH and adsorbed H_2O in the products, respectively.[23b] The strong peaks at 1418−1484 cm^{-1} are attributed to the ν_3 mode of carbonate CO_3^{2-} species, while the band at 1518 cm^{-1} might result from carboxylate groups. The minute bands appearing at 1070−863, 812, and 722−690 cm^{-1} are assigned to the ν_1, ν_2, and ν_4 modes of CO_3^{2-}, respectively. These observed very strong features in the spectrum of the **P2** sample substantiate the claim that the products are composed of $La(CO_3)OH$.[23c]

Morphology. The morphologies and dimensions of the products are summarized in Table 1 (Supporting Information). From Table 1 in the Supporting Information, it is found that the carbon sources and pH values of the initial reaction system are two categories of predominantly influencing factors in the determination of the shapes and sizes of the as-formed products, which will be discussed in the following paragraphs.

A. $CO(NH_2)_2$ as the Carbon Source. The scanning electron microscopy (SEM) images provide direct information about the sizes and typical shapes of the as-synthesized $LaCO_3OH$ products grown under different experimental conditions. Figure 2 shows the representative SEM images of the $LaCO_3OH$ products prepared using $CO(NH_2)_2$ as the carbon source at different pH values. The sample (**P1**) obtained at pH = 2 is composed of a great deal of elliptical

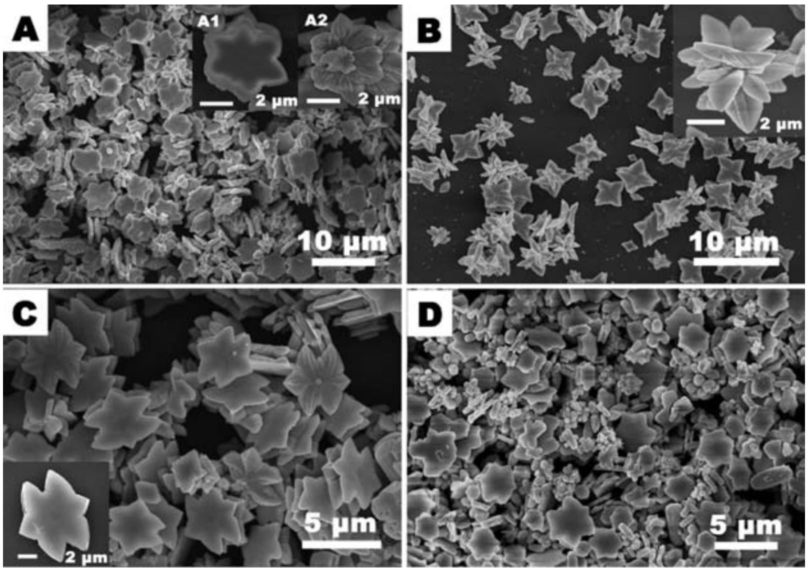

Figure 3. SEM images of $LaCO_3OH$ microcrystals obtained under different carbon sources and pH values: (A) $NaHCO_3$, pH = 7; (B) NH_4HCO_3, pH = 7; (C) $NaHCO_3$, pH = 10; (D) NH_4HCO_3, pH = 10. The insets are corresponding magnified micrographs.

nanoflakes and microflowers that consist of conjunctions of nanoflakes in terms of both edge-to-edge and edge-to-surface (Figure 2A,B). The lengths and thicknesses of these ellipselike nanoflakes are 3.5−5.0 μm and 10−30 nm, respectively, and the diameter of the microflowers is about 5.0 μm. When the pH value of the initial solution is not adjusted (pH = 7; **P2**), the morphology of the product varies greatly. It can be seen clearly from Figure 2C that there are a large number of perfect rhombic microplates with a size of 1.5−2.5 μm in side length and 100−200 nm in thickness. Interestingly, the top/bottom surfaces exhibit concave centers (Figure 2C, inset). The magnified SEM image (Figure 2D) clearly shows that the individual rhombic microplate has a highly smooth surface, equal side lengths, and uniform thickness. In addition, the EDX spectrum of **P2** reveals the presence of La, O, and C (H cannot be detected by this method), which is consistent with the results of XRD and FT-IR. When the pH value is increased to 10 with $NH_3 \cdot H_2O$ (25 wt %), the morphology of the product (**P3**) is converted to sandwichlike microspindles with 300−700 nm thickness and 2.0−3.0 μm length, as shown in Figure 2E. From its magnified SEM image (Figure 2F), it is found that a single spindle consists of two layers and the center thickness of the spindle is greater than the edge thickness, which results in the formation of a deeper concave than that of the **P2** sample. At the same time, a protuberant part appears in the short-axis direction of these microspindles. In summary, the morphologies undergo variations from elliptical nanoflakes to rhombic microplates and then to sandwichlike microspindles with increases of the pH values from 2 to 10 when using $CO(NH_3)_2$ as the carbon source. All of the experimental parameters except for the pH values of the initial solution are identical from the **P1** to **P3** samples, indicating that the difference of morphologies of the $LaCO_3OH$ products is caused by variation of the pH values.

B. $NaHCO_3$ and NH_4HCO_3 as the Carbon Sources. Upon substitution of $CO(NH_2)_2$ for $NaHCO_3$ and NH_4HCO_3 as the carbon source while keeping the other experimental parameters unchanged, the morphologies of the obtained $LaCO_3OH$ products have dramatic differences relative to the products obtained by using $CO(NH_2)_2$. Figure 3 depicts typical SEM images of the corresponding products (**P4**−**P7**) using $NaHCO_3$ and NH_4HCO_3 as the carbon sources and under different pH values. It can be seen clearly that when using $NaHCO_3$ as the carbon source and at pH = 7, double-deck-like microhexagrams with 4.0−5.5 μm diameter (the distance between two opposite vertexes) and 1.5−2.5 μm thickness are observed. The magnified SEM images of one isolated hexagram demonstrate the presence of six scrappy angles and rugate endothecium, as shown in the insets of Figure 3A. With an increase of the pH to 10, the morphology of $LaCO_3OH$ microcrystals is still a two-double hexagram. However, the higher resolution SEM image of individual hexagrams (Figure 3C, inset) shows that it is different from that obtained at pH = 7, of which the diameter and thickness shrink to 4.0−5.0 and 1.0−1.5 μm, respectively. If $CO(NH_2)_2$ is replaced by NH_4HCO_3 and with the pH value of the initial solution at 7, the obtained products present a flowerlike morphology with an approximate diameter of 4.0−7.0 μm. More careful examination of the magnified SEM image (Figure 3B, inset) shows clearly that these microflowers are composed of a lot of spinous protuberances. Moreover, when the experiment is performed at pH = 10, irregular microhexagrams and microflowers simultaneously are observed, indicating the higher pH values are disadvantageous to forming uniform and regular microcrystals when using NH_4HCO_3 as the carbon source.

C. Na_2CO_3 and $(NH_4)_2CO_3$ as the Carbon Sources. When Na_2CO_3 and $(NH_4)_2CO_3$ are used as the carbon sources and the other experimental conditions remain unchanged, the morphologies of the as-formed products are also different from those observed products using $CO(NH_2)_2$ as the carbon source, as shown in Figure 4. At pH = 7, irregular two-double microrhombic $LaCO_3OH$ products with an average size of 1.5 μm length and 0.75 μm thickness are observed by using Na_2CO_3 as the carbon source (Figure 4A). If the carbon source is $(NH_4)_2CO_3$ and the pH = 7, the obtained products are

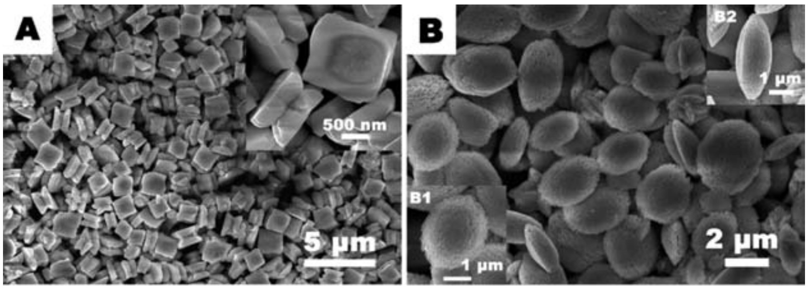

Figure 4. SEM images of $LaCO_3OH$ microcrystals at pH = 7 with different carbon sources: (A) Na_2CO_3; (B) $(NH_4)_2CO_3$.

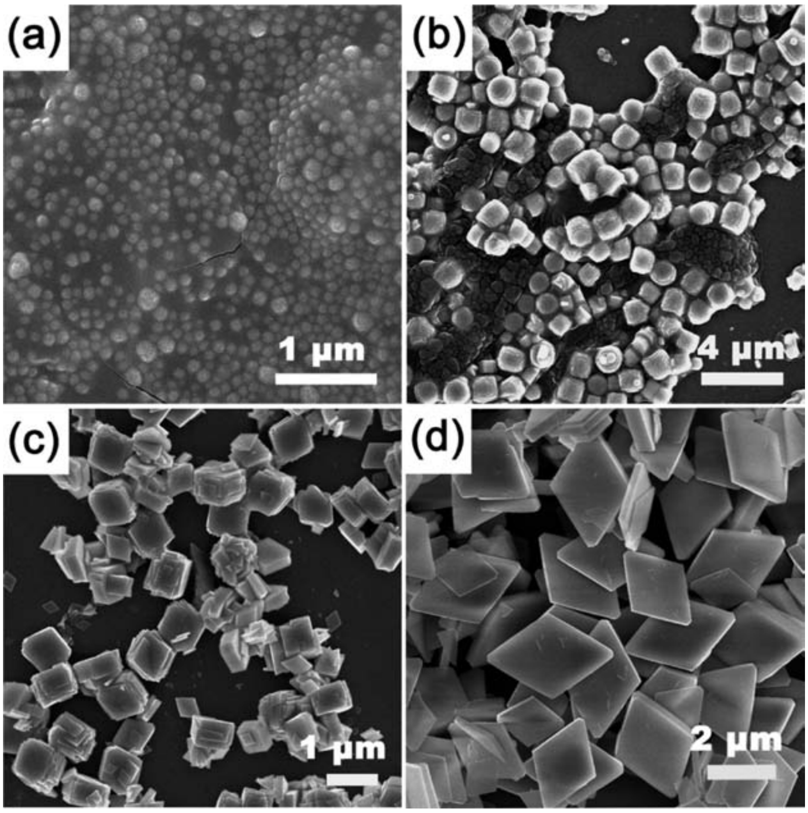

Figure 5. Typical SEM images of the **P2** product obtained at early stages. The corresponding reaction durations were (a) 10, (b) 30, (c) 60, (d) 120 min at 90 °C.

peach-nucleus-shaped microcrystals with 2.5−3.5 μm length and 1.0−1.5 μm center thickness. The magnified SEM image indicates that the single peach-nucleus-shaped microcrystal is composed of a great deal of smaller nanoparticles (Figure 4B1), which indicates that these microcrystals may originate from the self-assembly of these nanoparticles. Moreover, its center thickness is greater than the edge thickness (Figure 4B2). However, when using Na_2CO_3 and $(NH_4)_2CO_3$ as the carbon sources and the pH is adjusted to 10, the obtained products are all irregular microcrystals, as shown in Figure S3 (Supporting Information). This result indicates that the higher pH is also disadvantageous to forming well-defined microcrystals when using Na_2CO_3 and $(NH_4)_2CO_3$ as the carbon sources.

Growth Mechanism. In general, the growth of crystals and the formation of various morphologies are complex processes that are the cooperative result of inherent structures and external experimental conditions such as pH values in the initial solution, carbon sources, and so on. To gain a better understanding of the growth mechanism of the $LaCO_3OH$ products with multiform morphologies, the representative **P2** sample formed at early stages was collected for SEM analysis. It was found that, after reaction of the $La(NO_3)_3$ and $CO(NH_2)_2$ solution at 90 °C for 10 min, a white precipitate was formed. As seen from the SEM image shown in Figure 5a, the white precipitate is comprised of amorphous spherical nanoparticles. Moreover, the EDX spectrum indicates the presence of La, O, and C elements in the white precipitate. Therefore, it is believed that the perfect microrhombuses originated from these amorphous nanoparticles, which formed during the early growth stage. Interestingly, some hexagonal prisms with an average size of 1.5 μm length and 1.0 μm thickness were observed after an aging time of 30 min at 90 °C (Figure 5b), which possibly results from the inherent crystal structure of orthorhombic $LaCO_3OH$. With the reaction time prolonged to 60 min, the crystal continued to grow and formed some irregular rhombuses, as shown in Figure 5c. Finally, the morphology completely evolved to perfect microrhombuses (Figure 5d) after

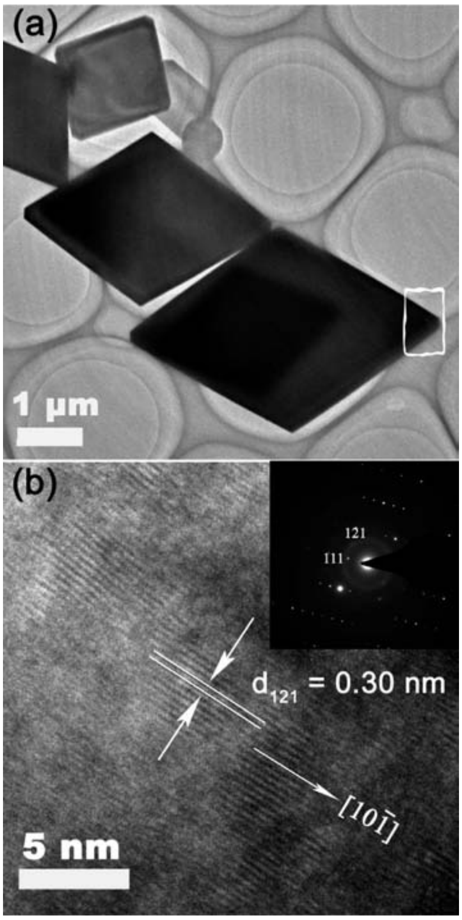

Figure 6. (a) TEM image of $LaCO_3OH$ rhombic microplates with $CO(NH_2)_2$ as the carbon source at pH = 7 and (b) the corresponding HRTEM image and SAED pattern obtained from a head region contained in the whole rectangle.

a reaction time of over 2 h. The whole process may be simply described by the following reactions:

$$CO(NH_2)_2 + 2H_2O \rightarrow CO_3^{2-} + 2NH_4^+$$

$$NH_3 \cdot H_2O \rightarrow NH_4^+ + OH^-$$

$$La^{3+} + CO_3^{2-} + OH^- \rightarrow LaCO_3OH$$

To further study the fine structure and examine the typical growth direction of the perfect $LaCO_3OH$ microrhombuses, TEM was performed. Figure 6A is a representative TEM image of an individual rhombic microplate parallel to the substrate. The very regular cross section can be clearly observed, indicating that the morphology of the as-prepared products presents a perfect rhombus. As disclosed by the corresponding high-resolution TEM (HRTEM) image (Figure 6B), which was taken with the electron beam perpendicular to the edge of the microplate, the sample is structurally uniform with interplanar distances of about 0.30 nm, which corresponds to the *d*-spacing value of the (121) planes. The SAED pattern of the **P2** sample (Figure 6d, inset) taken from the head region of a single rhombic microplate reveals its single-crystal structure, and the diffraction spots can be indexed as the (121) and (111) reflections of the orthorhombic $LaCO_3OH$ phase, in accordance with the XRD result. On the basis of the above results, it can be determined that the preferential growth orientation of the rhombic microplates is along [10$\bar{1}$]. Furthermore, the preferential growth direction of the $LaCO_3OH$ crystal varies with a change of the external experimental conditions, which results in the formation of multiform $LaCO_3OH$ products.

In conclusion, the above results indicate that the carbon sources and pH values are critical factors responsible for the final morphologies of the as-prepared $LaCO_3OH$ products; namely, different carbon sources and pH values induce the crystals to grow along different directions and form multiform $LaCO_3OH$ products. In addition, simple ions such as NH^{4+} and Na^+ have also different effects on the morphologies. When **P4** was compared with **P6**, **P5** with **P7**, or **P8** with **P10**, with the exception of the use of different carbon sources of $NaHCO_3$, NH_4HCO_3, Na_2CO_3, and $(NH_4)_2CO_3$, these $LaCO_3OH$ products with different morphologies were synthesized under identical reaction conditions of $[La^{3+}]$ = 0.5 M and the same pH value, reaction temperature, and time (90 °C, 2 h), indicating that the nature of the simple ions (NH^{4+} and Na^+) also contributes to the formation of various architectures. The cations NH_4^+ and Na^+ in the reaction system have a guiding effect on the changes in the microstructures of the as-prepared $LaCO_3OH$ crystals. Wang and co-workers had suggested that the cations coming from the different fluoride sources XF (X = K^+, H^+, NH_4^+, Na^+, Rb^+, and Cs^+) selectively adsorbed on the different crystal facets of EuF_3 nanoparticles, resulting in the formation of various shapes.[24] Other workers have found that the simple ions direct the growth of nanoparticles into different shapes, highlighting the importance of these species.[25] It is therefore reasonable to assume a similar situation for the effects of Na^+ andNH_4^+ on the morphologies. At the early stages of the reactions, because of strong interactions between Na^+ and NH_4^+ cations and CO_3^{2-} or HCO_3^{2-} anions, these two cations can be selectively adsorbed on specific facets of the initial $LaCO_3OH$ crystals and change their surface energy. However, because of the different ion radii of Na^+ and NH^{4+}, the relative growth rates of various crystal facets are different, leading to the formation of a variety of morphologies. Scheme 1 shows the possible formation mechanism for $LaCO_3OH$ nano/microcrystals with different morphologies under different carbon sources and pH values.

3.2. Phase Identification and Morphology of $La_2O_2CO_3$ and La_2O_3. Thermal decomposition of the homogeneously precipitated/hydrothermal precursor is a simple route toward tailored rare-earth and metal oxides.[26,27]

---

[24] (a) Wang, M.; Huang, Q. L.; Hong, J. M.; Chen, X. T.; Xue, Z. L. *Cryst. Growth Des.* **2006**, *6*, 1972. (b) Wang, M.; Huang, Q. L.; Hong, J. M.; Chen, X. T.; Xue, Z. L. *Cryst. Growth Des.* **2006**, *6*, 2169.

[25] (a) Xia, T.; Li, Q.; Liu, X. D.; Meng, J.; Cao, X. Q. *J. Phys. Chem. B* **2006**, *110*, 2006. (b) Li, C. X.; Quan, Z. W.; Yang, P. P.; Yang, J.; Lian, H. Z.; Lin, J. *J. Mater. Chem.* **2008**, *18*, 1353.

[26] (a) Yang, J.; Li, C. X.; Quan, Z. W.; Zhang, C. M.; Yang, P. P.; Li, Y. Y.; Yu, C. C.; Lin, J. *J. Phys. Chem. C* **2008**, *112*, 12777. (b) Xu, A. W.; Fang, Y. P.; You, L. P.; Liu, H. Q. *J. Am. Chem. Soc.* **2003**, *125*, 1494. (c) Wang, J. C.; Liu, Q.; Liu, Q. F. *J. Mater. Chem.* **2005**, *15*, 4141. (d) Bai, X.; Song, H. W.; Yu, L. X.; Yang, L. M.; Liu, Z. X.; Pan, G. H.; Lu, S. Z.; Ren, X. G.; Lei, Y. Q.; Fan, L. B. *J. Phys. Chem. B* **2005**, *109*, 15236.

[27] (a) Zhang, J.; Liu, Z. G.; Lin, J.; Fang, J. *Cryst. Growth Des.* **2005**, *5*, 1527. (b) Li, G. G.; Peng, C.; Li, C. X.; Yang, P. P.; Hou, Z. Z.; Fan, Y.; Cheng, Z. Y.; Lin, J. *Inorg. Chem.* **2010**, *49*, 1449. (c) Wang, X.; Li, Y. D. *Chem.—Eur. J.* **2003**, *9*, 5627. (d) Qiu, X. Q.; Li, G. S.; Li, L. P. *J. Mater. Res.* **2007**, *22*, 908.

Scheme 1. Schematic Illustration for the Possible Formation Process of $LaCO_3OH$ Microcrystals with Various Morphologies Using Different Carbon Sources of (a) $CO(NH_2)_2$, (b) $NaHCO_3$, (c) NH_4HCO_3, (d) Na_2CO_3, and (e) $(NH_4)_2CO_3$ and at Different pH Values (2, 7, and 10)

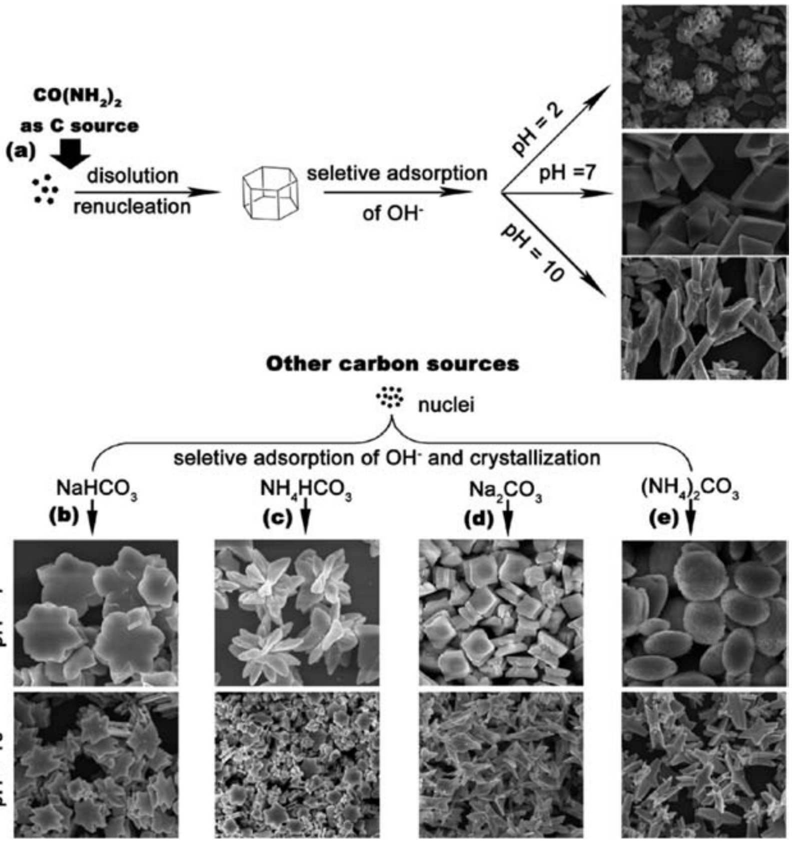

After the synthesis of the lanthanum carbonate hydroxide precursors, we employ **P1**−**P3** samples as examples to investigate the effect of calcination on the crystallization and morphology of the as-prepared products. Figure S4 (Supporting Information) shows TG-DTA curves of the representative **P2** sample. The results for the **P1** and **P3** samples are similar to those for the **P2** sample and will not be shown here. On the basis of TG-DTA data, it can be seen clearly that thermal decomposition of the $LaCO_3OH$ precursors undergoes two phase transformation processes when the temperature is elevated from room temperature to 800 °C. The first one is the transformation from $LaCO_3OH$ to $La_2O_2CO_3$ with the turning point at 480 °C, and the second one is the transformation from $La_2O_2CO_3$ to La_2O_3 with the turning point at 724 °C. Therefore, in order to obtain the corresponding $La_2O_2CO_3$ and La_2O_3 products, we calcined the **P1**−**P3** samples at 600 and 800 °C for 4 h, and the obtained products are denoted as **M1**−**M3** and **N1**−**N3**, respectively. Figure S5 in the Supporting Information shows the XRD patterns of the **M1**−**M3** samples. The diffraction peaks of **M2** and **M3** can be readily indexed to a pure hexagonal $La_2O_2CO_3$ phase [space group $P63/mmc$ (No. 194)] according to JCPDS no. 37-0804, while that of **M1** is assigned to a pure monoclinic $La_2O_2CO_3$ phase (JCPDS no. 48-1113). No additional peaks of other phases have been found, indicating that the $LaCO_3OH$ precursors were completely converted to $La_2O_2CO_3$ at 600 °C for 4 h. When the **P1**−**P3** samples were calcined at 800 °C for 4 h, the XRD patterns of **N1**−**N3** samples are all indexed to a pure hexagonal La_2O_3 phase [space group $P3\overline{m}1$ (No. 164)], which coincides very well with JCPDS no. 05-0602, as shown in Figure S6 in the Supporting Information. No second phase appears, indicating that $LaCO_3OH$ was completely converted to La_2O_3 at 800 °C for 4 h. In summary, the phase transformation processes can be simply depicted as follows:

$$2LaCO_3OH \xrightarrow{873\ K} La_2O_2CO_3 + CO_2 + H_2O$$

$$La_2O_2CO_3 \xrightarrow{1073\ K} La_2O_3 + CO_2$$

Figure 7 shows typical SEM, TEM, and HRTEM images of $La_2O_2CO_3$ (**M2**) and La_2O_3 (**N2**) samples. From Figure 7a−d, it can be seen that the $La_2O_2CO_3$ and La_2O_3 samples inherited their parents' morphologies, but their size was slightly shrunk in comparison with the $LaCO_3OH$ products in that the density of the former is higher than that of the latter. $LaCO_3OH$ was converted to $La_2O_2CO_3$ and La_2O_3, and their surfaces became rough during subsequent calcination processes at different temperatures with the gradual elimination of H_2O and CO_2. Nevertheless, conversion did not lead to changes in the morphologies. Such a transformation was common for rare-earth hydroxide and other metal compound decomposition.[26b,d,27a,27b] The morphologies were maintained perhaps because of the higher activation energies needed for the collapse of these structures.[28] The same situation holds for other $La_2O_2CO_3$ and La_2O_3 samples such as **M1**, **M3**, **N1**, and **N3** samples,

---

[28] (a) Yang, J.; Quan, Z. W.; Kong, D. Y.; Liu, X. M.; Lin, J. *Cryst. Growth Des.* **2007**, *7*, 730. (b) Yang, J.; Lin, C. K.; Wang, Z. L.; Lin, J. *Inorg. Chem.* **2006**, *45*, 8973.

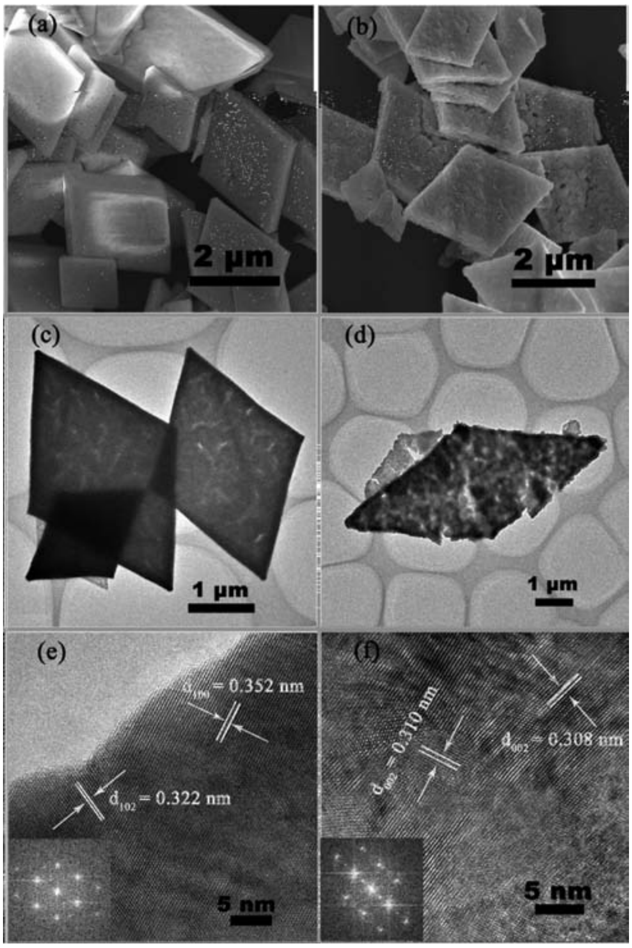

Figure 7. (a) SEM, (c) TEM, and (e) HRTEM images for the $La_2O_2CO_3$ sample (**M2**). (b) SEM, (d) TEM, and (f) HRTEM images for the La_2O_3 sample (**N2**). The insets show their corresponding FT-IR images from HRTEM images.

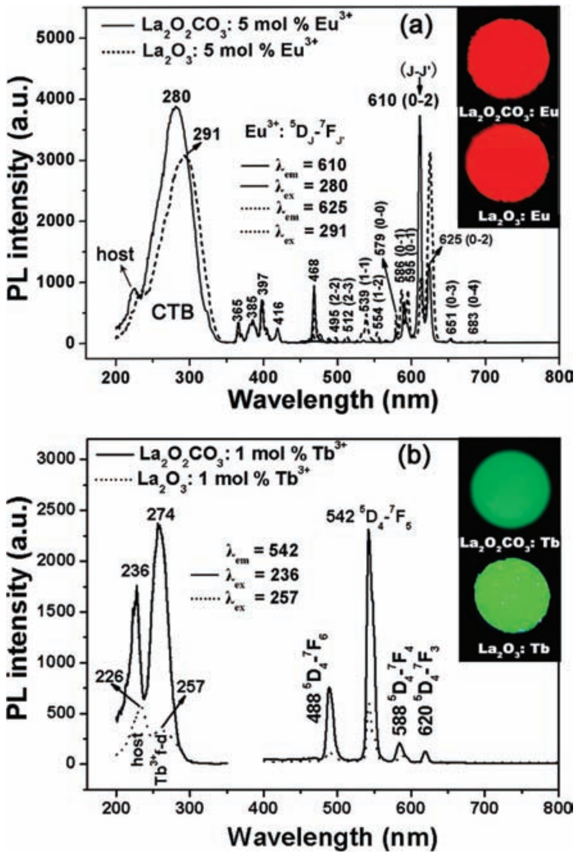

Figure 8. PL excitation and emission spectra of (a) $La_2O_2CO_3:Eu^{3+}$ (5 mol %; solid line) and $La_2O_3:Eu^{3+}$ (5 mol %; dashed line) and (b) $La_2O_2CO_3:Tb^{3+}$ (1 mol %; solid line) and $La_2O_3:Tb^{3+}$ (1 mol %; dashed line) with rhombic shape. The insets are their corresponding luminescence photographs under 254 nm UV light excitation.

of which the corresponding SEM images are shown in Figure S7 (Supporting Information). In addition, the SEM and TEM images of the **M2** and **N2** samples also indicate that these microrhombuses were further composed of fine and closely linked nanoparticles with a size range from several tens to hundreds of nanometers, which is consistent with the above growth mechanism of lanthanum carbonate hydroxides. The fine structures of the **M2** and **N2** samples were studied by the HRTEM technique. Figure 7e is the corresponding HRTEM image for the **M2** sample, in which the lattice fringes show the imaging characteristics of the $La_2O_2CO_3$ crystal where *d* spacings of 0.352 and 0.322 nm correspond to the distances of the (100) and (102) planes, respectively. The HRTEM images (Figure 7f) of the **N2** sample clearly show lattice fringes with interplanar spacings of 0.310 and 0.308 nm, which all correspond to the (002) plane of La_2O_3. The FT-IR images for the **M2** and **N2** samples indicate that they are hexagonal $La_2O_2CO_3$ and La_2O_3 structures, respectively. These results further confirm the presence of highly crystalline $La_2O_2CO_3$ and La_2O_3 phases after annealing of $LaCO_3OH$ at a suitable heat treatment, agreeing well with the XRD results.

3.3. Luminescence Properties. **PL Properties of $La_2O_3CO_3/La_2O_3:Eu^{3+}$ or Tb^{3+}.** Our experimental results and previous reports have shown that $La_2O_2CO_3$ and La_2O_3 are good host materials for the luminescence of various optically activated lanthanide ions.[15,16] In addition, it should be mentioned that the existence of other lanthanide ions in $La_2O_2CO_3$ and La_2O_3 did not change the phase, crystallization, and morphology of the products in our present work. Accordingly, we mainly focused on the luminescence properties of Eu^{3+}- and Tb^{3+}-doped $La_2O_2CO_3$ and La_2O_3 nano/microstructures, in an effort to reveal that our current homogeneous precipitation method following a heat treatment process is a facile and efficient process for the preparation of carbonate oxide and oxide phosphors with multinovel morphologies. Herein the $La_2O_2CO_3/La_2O_3$: Eu^{3+} or Tb^{3+} samples with rhombic microplate shapes were used as representative examples to investigate their PL and CL properties. The doping concentrations of Eu^{3+} and Tb^{3+} in $La_2O_2CO_3$ and La_2O_3 hosts have been optimized in our experiments and were 5, 5, 1, and 1 mol % of La^{3+}, respectively. Upon 254 nm UV light radiation, these phosphors show bright red, red, green, and green luminescence to the naked eye, respectively, and the corresponding luminescence digital photographs are shown as the insets.

Figure 8 shows the PL excitation and emission spectra of $La_2O_2CO_3:Eu^{3+}$ (5 mol %), $La_2O_3:Eu^{3+}$ (5 mol %), $La_2O_2CO_3:Tb^{3+}$ (1 mol %), and $La_2O_3:Tb^{3+}$ (1 mol %) samples. Detailed assignments for the excitation and emission peaks and luminescent properties, for example, CIE chromaticity coordinates, lifetimes, QY, emission colors, and so on, are listed in Table 2 (Supporting Information).

The excitation spectrum of $La_2O_2CO_3:Eu^{3+}$ (5 mol %; Figure 8a, solid line) monitored with 610 nm shows two broad excitation bands (the weak one with a range from 200 to 234 nm centered at 226 nm and the strong one with a range from 234 to 350 nm centered at 280 nm) and a number of line excitation peaks (the strongest one is located at 468 nm for the $^7F_0 \rightarrow {}^5D_2$ transition) of Eu^{3+}. The strong band centered at 280 nm is due to the charge-transfer transition between O^{2-} and Eu^{3+},[29] and the weak broad band peaking at 226 nm should be ascribed to the host absorption.[30] Upon excitation with 280 nm UV, the $La_2O_2CO_3:Eu^{3+}$ (5 mol %) sample shows a strong red luminescence, and the corresponding emission spectrum consists of the characteristic transitions of Eu^{3+} within its $4f^6$ configuration, i.e., $^5D_1 \rightarrow {}^7F_1$ (535 nm), $^5D_0 \rightarrow {}^7F_0$ (580 nm), $^5D_0 \rightarrow {}^7F_1$ (590 nm), $^5D_0 \rightarrow {}^7F_2$ (610, 625 nm), and $^5D_0 \rightarrow {}^7F_3$ (653 nm). The strongest one is located at 610 nm. For the $La_2O_3:Eu^{3+}$ (5 mol %) sample, the excitation spectrum (monitored by $Eu^{3+5}D_0 \rightarrow {}^7F_2$ at 625 nm; Figure 8a, left dashed line) consists of a intense broad band from 250 to 330 nm with the maximum at 291 nm, a weak broad band from 200 to 250 nm with the peak around 230 nm, and some Eu^{3+} excitation peaks. The broad band around 291 nm is also attributed to the charge-transfer band (CTB) of $Eu^{3+}-O^{2-}$,[29] and the band peaking around 230 nm is related to the host excitation, i.e., electronic transitions from the O 2p valence band to the La 5d6s conduction band.[30] The emission spectrum of La_2O_3: Eu^{3+} (5 mol %; Figure 10a, right dashed line) obtained by excitation into 291 nm contains exclusively the characteristic emission of Eu^{3+}, as shown in Table 2 in the Supporting Information. On the basis of the above analyses, it can be clearly seen that there are two great differences in the PL spectra of the $La_2O_2CO_3:Eu^{3+}$ (5 mol %) and $La_2O_3:Eu^{3+}$ (5 mol %) samples, as follows: First, the excitation peak of $La_2O_3:Eu^{3+}$ (5 mol %) moved 11 nm to a shorter-wavelength direction than that of $La_2O_2CO_3:Eu^{3+}$ (5 mol %). Second, the $^5D_0 \rightarrow {}^7F_2$ transition intensity ratio of 625 to 610 nm is greatly enhanced in $La_2O_3:Eu^{3+}$ (5 mol %) in comparison with that in $La_2O_2CO_3:Eu^{3+}$ (5 mol %).

For RE-doped luminescence materials, the local environment of the activator ions is believed to have a crucial impact on the luminescence behavior, and it is important to explain the differences in the spectra of different microstructures. There are many reports on studies of the site symmetry of activators of the RE-doped luminescence materials,[31] while the corresponding systematic research on Eu-doped $La_2O_2CO_3$ and La_2O_3 phosphors has not been achieved. Eu^{3+} ($4f^6$ configuration) is widely used as a probe of the surrounding symmetry because the emission and excitation lines between the $^5D_0$ and $^7F_0$ levels are nondegenerate. This reveals the presence of crystallographic nonequivalent sites in a given host matrix.[32] The site-selective excitation spectroscopic technique (dye laser with a continuous wavelength in the region of $^7F_0 \rightarrow {}^5D_0$ of Eu^{3+}) is a good method to investigate the distribution of metal cations at different atomic sites in a microstructure, which plays a significant role in tailoring the physical properties of the material for device applications. In this work, the different Eu^{3+} sites in the $La_2O_2CO_3$ and La_2O_3 host lattices were selectively excited with a tunable dye laser and the luminescence spectra of each site were recorded separately. Parts a and b of Figure 9 show the excitation spectra corresponding to the $^7F_0 \rightarrow {}^5D_0$ transition in $La_2O_2CO_3$ and La_2O_3 matrices, respectively, obtained by monitoring the $^5D_0 \rightarrow {}^7F_2$ transition at 20 and 300 K. The excitation spectrum of $La_2O_2CO_3:Eu^{3+}$ (5 mol %) microrhombus sample consists of two strong peaks at 579.0 and 580.3 nm as well as a weak peak at 580.8 nm, which are denoted as Eu^{3+} (M_1), Eu^{3+} (M_2), and Eu^{3+} (M_3), respectively. No other line corresponding to the $^7F_0 \rightarrow {}^5D_0$ transition was detected at temperatures of 20 and 300 K. The occupation probability of the major sites Eu^{3+} (M_1) and Eu^{3+} (M_2) is dominant. The minor site Eu^{3+} (M_3) is weakly occupied because of its weak excitation intensity. The results in Figure 9a clearly indicate that the Eu^{3+} ions occupy three different intrinsic crystallographic sites in the $La_2O_2CO_3$ matrix, which is consistent with the previous report.[33] For the $La_2O_3:Eu^{3+}$ (5 mol %) microrhombus sample, its excitation spectrum monitored at 20 K consists of the strongest line at 580.9 nm and two weak peaks at 579.2 and 581.3 nm, which are labeled as Eu^{3+} (N_2), Eu^{3+} (N_1), and Eu^{3+} (N_3), respectively. The occupation probability of the major site Eu^{3+} (N_2) is dominant, and the minor sites Eu^{3+} (N_1) and Eu^{3+} (N_3) are weakly occupied because of its weak excitation intensity. The results in Figure 9b clearly show that there is only one intrinsic crystallographic site of La^{3+} for the Eu^{3+} ions in the La_2O_3 matrix, which is also consistent with the previous report.[34] The other Eu^{3+} ions may exist in the term of the cluster of Eu^{3+} ions.[35] However, the weak excitation peaks of $La_2O_3:Eu^{3+}$ (5 mol %; 579.2 and 581.3 nm) disappear when the monitoring temperature is elevated to 300 K, and there is only a strong line at 580.5 nm. The possible reason is that the heat movement swells between the adjacent ions and temperature quenching occurs with an increase of the monitoring temperature.

In addition, the site-selective emission spectra under the M_1, M_2, and M_3 line excitations for $La_2O_2CO_3:Eu^{3+}$ (5 mol %) and N_1, N_2, and N_3 line excitations for La_2O_3: Eu^{3+} (5 mol %) at 20 and 300 K are also shown in parts c and d of Figure 9, respectively. The different emission

---

(29) (a) Park, J. K.; Park, S. M.; et al. *J. Mater. Sci. Lett.* **2001**, *20*, 2231. (b) Lin, C. C.; Liu, R. S.; Tang, Y. S.; Hu, S. F. *J. Electrochem. Soc.* **2008**, *155*, J248. (c) Ghys, J. D.; Mauricot, R.; Caillier, B.; Guillot, P.; Beaudette, T.; Jia, G. H.; Tanner, P. A.; Cheng, B. M. *J. Phys. Chem. C* **2010**, *114*, 6681. (d) Fernandes, J. A.; Ferreira, R. A. S.; Pillinger, M.; Carlos, L. D.; Gonçalves, I. S.; Ribeiro-Claro, P. J. A. *Eur. J. Inorg. Chem.* **2004**, *19*, 3913.

(30) Prokofiev, A. V.; Shelykh, A. I.; Melekh, B. T. *J. Alloys Compd.* **1996**, *242*, 41.

(31) (a) Jia, C. J.; Sun, L. D.; Yan, Z. G.; Pang, Y. C.; L. S. Z.; Yan, C. H. *Eur. J. Inorg. Chem.* DOI: 10.1002/ejic.201000038. (b) Lehmann, O.; Kömpe, K.; Haase, M. *J. Am. Chem. Soc.* **2004**, *126*, 14935. (c) Song, H. W.; Yu, L. X.; Lü, S. Z.; Wang, T.; Liu, Z. X.; Yang, L. M. *Appl. Phys. Lett.* **2004**, *85*, 470. (d) Sudarsan, V.; van Veggel, F. C. J. M.; Herring, R. A.; Raudsepp, M. *J. Mater. Chem.* **2005**, *15*, 1332. (e) Jia, G. H.; Tanner, P. A.; Duan, C. K.; Dexpert-Ghys, J. *J. Phys. Chem. C* **2010**, *114*, 2769.

(32) (a) Gorller-Walrand, C.; Binnemans, K. In *Handbook on the Physics and Chemistry of Rare Earths*; Gschneidner, K. A., Jr., Eyring, L., Eds.; North-Holland: Amsterdam, The Netherlands, 1996; Vol. *23*. (b) Liu, Y. S.; Luo, W. Q.; Li, R. F.; Chen, X. Y. *Opt. Lett.* **2007**, *32*, 566. (c) Luo, W. Q.; Li, R. F.; Liu, G. K.; Antonio, M. R.; Chen, X. Y. *J. Phys. Chem. C* **2008**, *112*, 10370.

(33) Paul Attfield, J.; Férey, G. *J. Solid State Chem.* **1989**, *82*, 132.

(34) Hoefdraad, H. E. *Chem. Phys. Lett.* **1975**, *32*, 216.

(35) (a) Zhang, S. Y.; Huang, Y. L.; Jin Seo, H. *J. Electrochem. Soc.* **2010**, *157*, J186. (b) Jin Seo, H.; Tsuboi, T.; Jang, K. W. *Phys. Rev. B* **2004**, *70*, 205113. (c) Huang, Y. L.; Cao, Y. Q.; Jiang, C. F.; Shi, L.; Tao, Y.; Jin Seo, H. *Jpn. J. Appl. Phys.* **2008**, *47*, 6364.

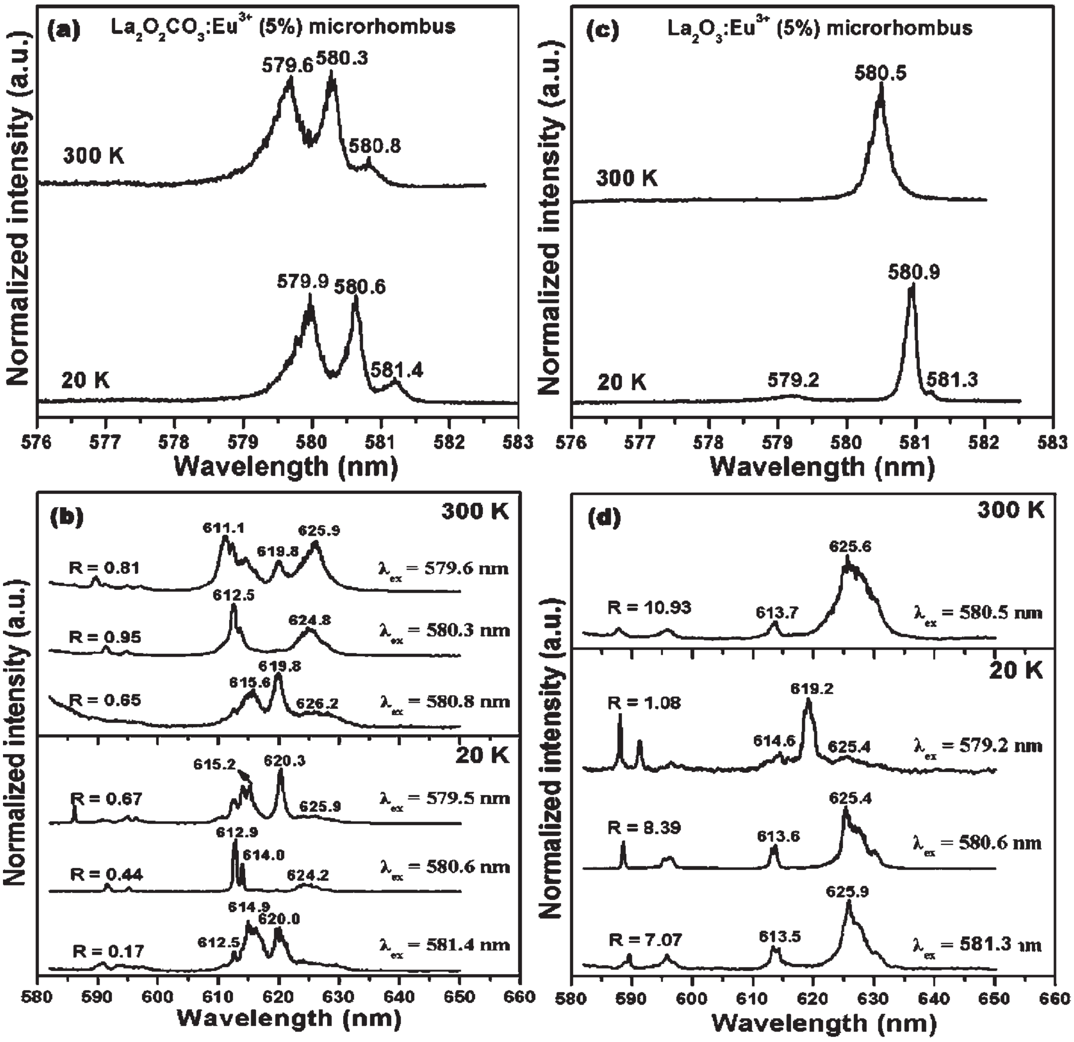

Figure 9. Excitation spectra in the region of the $^7F_0 \rightarrow {}^5D_0$ transition in (a) $La_2O_2CO_3$:Eu^{3+} (5 mol %) and (b) La_2O_3:Eu^{3+} (5 mol %) microrhombus samples at 20 and 300 K. Site-selective emission spectra of $^5D_0 \rightarrow {}^7F_2$ under different site-selective excitations into Eu^{3+} in (c) $La_2O_2CO_3$:Eu^{3+} (5 mol %) and (d) La_2O_3:Eu^{3+} (5 mol %) microrhombus samples at 20 and 300 K.

spectra in $La_2O_2CO_3$ and La_2O_3 host lattices for the $^5D_0 \rightarrow {}^7F_2$ transition are observed. For $La_2O_2CO_3$:Eu^{3+} (5 mol %), the emission spectra obtained at 300 K are similar to those at 20 K, which all show a higher $^5D_0 \rightarrow {}^7F_2$ emission intensity around 625 nm than around 610 nm. In contrast, the $^5D_0 \rightarrow {}^7F_2$ emission intensity around 625 nm is much lower than that around 610 nm for La_2O_3:Eu^{3+} (5 mol %) at 20 and 300 K except for the site-selective excitation in Eu^{3+} (N_1) having an equivalent value (R = 1.01) that may be due to the different Eu^{3+} ion clusters from the Eu^{3+} (N_3) site. Because of the morphology, the size and Eu^{3+}-doped concentration are basically identical for the $La_2O_2CO_3$:Eu^{3+} (5 mol %) and La_2O_3:Eu^{3+} (5 mol %) microrhombus samples, so these discrepancies should be attributed to their different microstructures, which results in Eu^{3+} ions locating in different crystal symmetries and coordination environments in the $La_2O_2CO_3$ and La_2O_3 hosts. Figure S8 in the Supporting Information shows 3D model structures and coordination environments with oxygen atoms of $La_2O_2CO_3$ and La_2O_3. $La_2O_2CO_3$ is believed to have layerlike structures, containing 2D $(La_2O_2^{2+})_n$ layers held together by CO_3^{2-} groups, as shown in Figure S8a in the Supporting Information. Similarly, La_2O_3 can also be considered as 2D $(La_2O_2^{2+})_n$ layers connected with O^{2-} ions. Because the size of CO_3^{2-} is bigger than that of O^{2-}, the average Eu–O distance in $La_2O_2CO_3$ is larger than that in La_2O_3, which results in CTB of Eu^{3+} in the former moving to high energy. This is the reason that the excitation peak of $La_2O_2CO_3$:Eu^{3+} (5 mol %) locates at 280 nm, which moves 11 nm to a shorter-wavelength direction relative to that of La_2O_3:Eu^{3+} (5 mol %). Furthermore, it can be seen clearly from Figure S8c in the Supporting Information that there are seven oxygen atoms coordinated with La^{3+} ions in La_2O_3. Strong $^5D_0 \rightarrow {}^7F_2$ emissions appear at approximately 625 nm because of Eu^{3+} present in the hexagonal La_2O_3 lattice with C_{3v} symmetry. When O^{2-} ions are replaced with CO_3^{2-} groups, the coordinated O^{2-} ions with La^{3+} ions increase to 10 in the $La_2O_2CO_3$ host, which make the Eu^{3+} ions have a lower symmetry in La_2O_3 compared with those in $La_2O_2CO_3$. Because of the hypersensitivity of the $^5D_0 \rightarrow {}^7F_2$ transition of Eu^{3+}, the environment has a crucial effect on the relative intensity of different $^5D_0 \rightarrow {}^7F_2$ emission peaks. Si et al.[36] reported

---

[36] (a) Si, R.; Zhang, Y. W.; You, L. P.; Yan, C. H. *Angew. Chem., Int. Ed.* **2005**, *44*, 3256. (b) Si, R.; Zhang, Y. W.; Zhou, H. P.; Sun, L. D.; Yan, C. H. *Chem. Mater.* **2007**, *19*, 18.

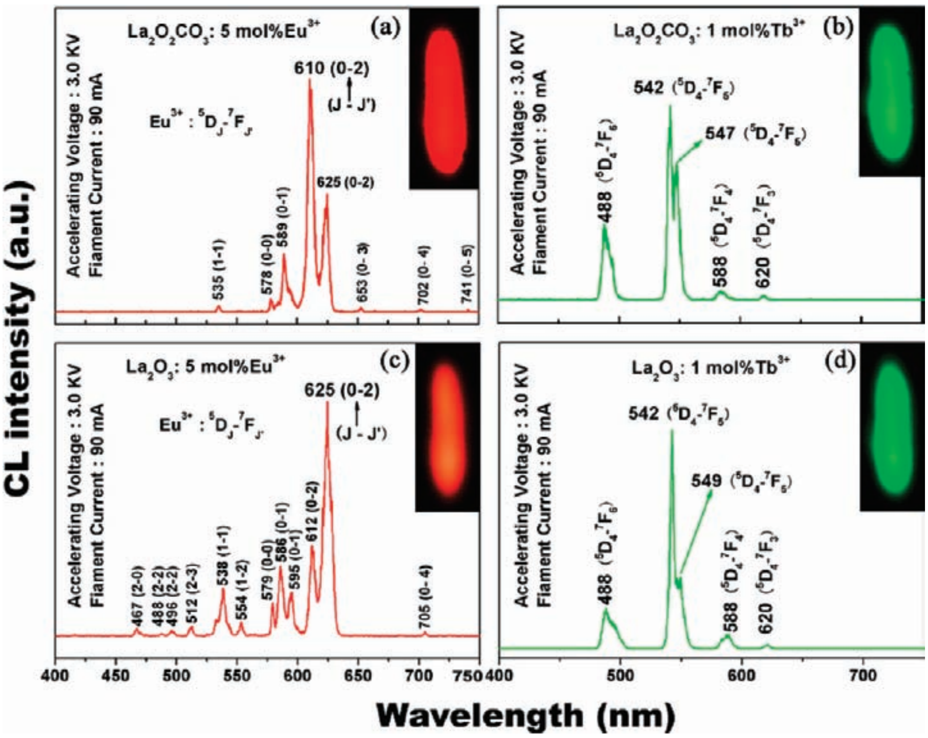

Figure 10. Typical CL spectra of (a) $La_2O_2CO_3$:Eu^{3+} (5 mol %), (b) $La_2O_2CO_3$:Tb^{3+} (1 mol %), (c) La_2O_3:Eu^{3+} (5 mol %), and (d) La_2O_3:Tb^{3+} (1 mol %) samples with rhombic microplate shapes. The insets are their corresponding luminescence photographs under 3.0 kV voltage electron-beam excitation.

that enhancement of the intensity ratio of the peak at 625 nm to the peak at 610 nm in Eu_2O_3 nanodisks in comparison with that of the Eu_2O_3 bulk materials is due to the lower symmetry of Eu^{3+} in the former, which is consistent with our observation. Because Eu^{3+} ions substitute for La^{3+} in $La_2O_2CO_3$ and La_2O_3, they have a lower symmetry in La_2O_3 than in $La_2O_2CO_3$, which results in a great enhancement of the intensity ratio of the peak at 625 nm to the peak at 610 nm of the $^5D_0 \rightarrow {}^7F_2$ transition of Eu^{3+}.

The luminescence decay curves of the $^5D_0 \rightarrow {}^7F_2$ emission after the M_1-M_3 and N_1-N_3 line excitations at different temperatures (20, 100, 200, and 300 K) were measured. All of the exponential decay curves can be fitted into a single-exponential function as $I = I_0 \exp(-t/\tau)$, where I_0 is the initial emission intensity for $t = 0$ and τ is the lifetime. The detailed luminescence lifetimes of Eu^{3+} ions are listed in Table 3 (Supporting Information). For $La_2O_2CO_3$:Eu^{3+} (5 mol %), the $^5D_0$ decay times in the M_1 and M_3 sites decrease with an increase of the temperature, presenting a typical temperature-quenching behavior, while the $^5D_0$ decay time in the M_2 site is close to a constant 0.87 ms from 20 to 300 K, indicating a relatively steady luminescence site. Similarly, for La_2O_3:Eu^{3+} (5 mol %), the N_2 site is a relatively steady luminescence center. Because the $^5D_0$ decay time in the N_2 site basically maintains a constant 0.72 ms, while those of in the N_1 and N_3 sites continuously decrease with an increase in the temperature from 20 to 300 K. The temperature-quenching behavior of the $^5D_0$ decay time in the N_1 and N_3 sites are obvious, as shown in Table 3 in the Supporting Information. The results are consistent with those of the excitation and site-selective emission spectra.

On the other hand, the $La_2O_2CO_3$:Tb^{3+} (1 mol %) and La_2O_3:Tb^{3+} (1 mol %) phosphors show similar emission spectral profiles, which are all attributed to $^5D_4 \rightarrow {}^7F_J$ (J = 6, 5, 4, 3) transitions of Tb^{3+} corresponding to $^5D_4 \rightarrow {}^7F_6$ (488 nm), $^5D_4 \rightarrow {}^7F_5$ (542 and 548/549 nm), $^5D_4 \rightarrow {}^7F_4$ (588 nm), and $^5D_4 \rightarrow {}^7F_3$ (620 nm), respectively, as shown in Figure 8b.[37] The strongest emissions all locate at 542 nm and are indexed to the $^5D_4 \rightarrow {}^7F_5$ transition of Tb^{3+}. Upon monitoring with the 542 nm emission, the excitation spectra of $La_2O_2CO_3$:Tb^{3+} (1 mol %) and La_2O_3:Tb^{3+} (1 mol %) all consist of two broad bands. The former broad band is attributed to the host absorption, and the latter broad band is due to the $4f^8-4f^75d^1$ transition of Tb^{3+}. However, there are some differences in the range and maximum of the two excitation bands in the $La_2O_2CO_3$ and La_2O_3 hosts. The excitation spectrum of the $La_2O_2CO_3$:Tb^{3+} (1 mol %) ranges from 200 to 300 nm with a maximum at 257 nm, while that of La_2O_3:Tb^{3+} (1 mol %) ranges from 200 to 320 nm with a maximum at 236 nm. All of these differences can be attributed to the different coordination environments and symmetries around the Tb^{3+} ions in the $La_2O_2CO_3$ and La_2O_3 hosts.

In summary, the microstructures (coordination environment and symmetry) of $La_2O_2CO_3$ and La_2O_3 have a crucial effect on Eu^{3+} or Tb^{3+} luminescence properties. The above investigations not only provide important experimental evidence for RE luminescence studies but also disclose the correlation between the microstructure and luminescence behavior, which could be used as a guide to the design and synthesis of novel luminescence materials.

CL Properties of $La_2O_3CO_3$/La_2O_3:Eu^{3+} or Tb^{3+}. In order to explore the potential of the as-synthesized

---

[37] Granadeiro, C. M.; Ferreira, R. A. S.; Soares-Santos, P. C. R.; Carlos, L. D.; Trindade, T.; Nogueira, H. I. S. *J. Mater. Chem.* **2010**, *20*, 3313.

$La_2O_2CO_3/La_2O_3:Eu^{3+}$ or Tb^{3+} samples to be used as CL materials, their CL properties have been investigated in detail. The $La_2O_2CO_3/La_2O_3:Eu^{3+}$ or Tb^{3+} products are stable under electron-beam excitation. Parts a−d of Figure 10 show typical CL spectra of the representative $La_2O_2CO_3:Eu^{3+}$ (5 mol %), $La_2O_2CO_3:Tb^{3+}$ (1 mol %), $La_2O_3:Eu^{3+}$ (5 mol %), and $La_2O_3:Tb^{3+}$ (1 mol %) samples with rhombic microplate shape, respectively, the profiles of which are similar to those of their PL spectra. Under low-voltage electron-beam excitation, $La_2O_2CO_3:Eu^{3+}$ (5 mol %) and $La_2O_3:Eu^{3+}$ (5 mol %) show the characteristic emission of Eu^{3+} ($^5D_J \rightarrow {}^7F_{J'}$, where $J = 0, 1, 2$ and $J' = 1-5$), and $La_2O_2CO_3:Tb^{3+}$ (1 mol %) and $La_2O_3:Tb^{3+}$ (1 mol %) exhibit the $^5D_4 \rightarrow {}^7F_J$ ($J = 3, 4, 5, 6$) characteristic transitions within the Tb^{3+} $4f^8$ electron configuration, as shown in Figure 10a−d. During excitation with 3.0 kV voltage, the above $La_2O_2CO_3:Eu^{3+}$ (5 mol %), $La_2O_2CO_3:Tb^{3+}$ (1 mol %), $La_2O_3:Eu^{3+}$ (5 mol %), and $La_2O_3:Tb^{3+}$ (1 mol %) samples respectively show bright red, red, green, and green luminescence to the naked eye, as depicted in the luminescent photographs from the insets in Figure 10a−d, and their corresponding CIE chromaticity coordinates are determined to be ($x = 0.6260$, $y = 0.3503$), ($x = 0.2521$, $y = 0.6052$), ($x = 0.5463$, $y = 0.3947$), and ($x = 0.2682$, $y = 0.6366$), respectively.

The CL emission intensities of the $La_2O_2CO_3:Eu^{3+}$ (5 mol %), $La_2O_2CO_3:Tb^{3+}$ (1 mol %), $La_2O_3:Eu^{3+}$ (5 mol %), and $La_2O_3:Tb^{3+}$ (1 mol %) samples with rhombic shape also have been investigated as a function of the accelerating voltage and the filament current, as shown in Figure 11. When the filament current is fixed at 90 mA, the CL intensity increases with an increase in the accelerating voltage from 1.5 to 3.5 kV (Figure 11a). Similarly, under a 3.0 kV voltage electron-beam excitation, the CL intensity also increases with an increase in the filament current from 85 to 97 mA (Figure 11b). The increase in the CL brightness with an increase in the electron energy and filament current is attributed to the deeper penetration of the electrons into the phosphor body and the larger electron-beam current density. The electron penetration depth can be estimated using the empirical formula $L\,[\text{Å}] = 250(A/\rho)(E/Z^{1/2})^n$, where $n = 1.2/(1-0.29 \log Z)$, A is the atomic or molecular weight of the material, ρ is the bulk density, Z is the atomic number or the number of electrons per molecule in the case of compounds, and E is the accelerating voltage (kV).[38] For $La_2O_2CO_3:Eu^{3+}$ (5 mol %), $La_2O_2CO_3:Tb^{3+}$ (1 mol %), $La_2O_3:Eu^{3+}$ (5 mol %), and $La_2O_3:Tb^{3+}$ (1 mol %) samples, the estimated electron penetration depth at 3.0 kV is about 5.8, 6.6, 5.9, and 6.7 nm, respectively. For CL, the Eu^{3+} and Tb^{3+} ions are excited by the plasma produced by the incident electrons. The deeper the electron penetration depth, the more plasma will be produced, which results in more Eu^{3+} and Tb^{3+} ions being excited and, thus, an increase in the CL intensity. From Figure 11, it can be seen that the $La_2O_2CO_3:Eu^{3+}$ (5 mol %) sample always has a higher CL intensity than the La_2O_3:5 mol % Eu^{3+} sample under the same excitation conditions, indicating that $La_2O_2CO_3$ is a better host than La_2O_3 for the Eu^{3+} ion doping. The same situation is available to the $La_2O_2CO_3:Tb^{3+}$ (1 mol %) and $La_2O_3:Tb^{3+}$ (1 mol %) samples.

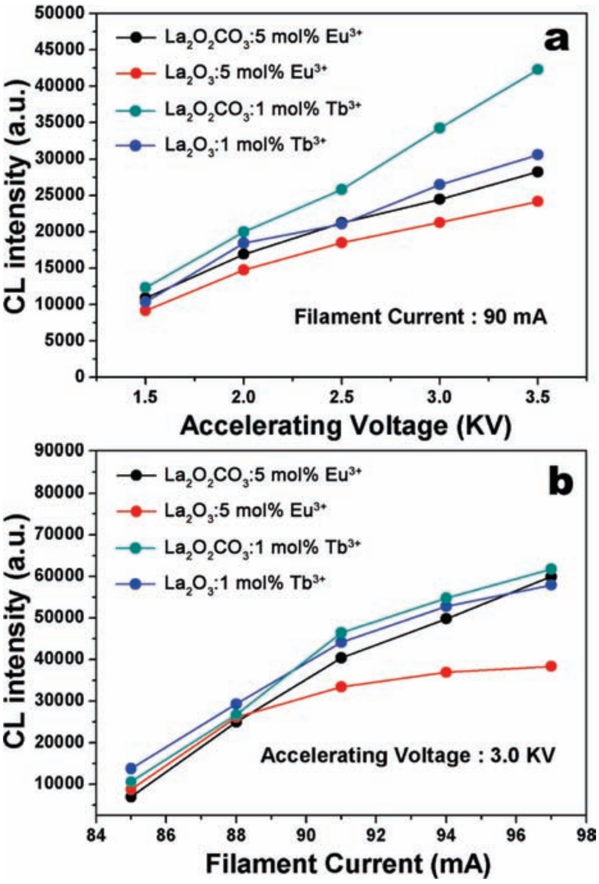

Figure 11. CL intensities of the $La_2O_2CO_3:Eu^{3+}$ (5 mol %), $La_2O_2CO_3:Tb^{3+}$ (1 mol %), $La_2O_3:Eu^{3+}$ (5 mol %), and $La_2O_3:Tb^{3+}$ (1 mol %) samples with rhombic shape as a function of (a) accelerating voltage and (b) filament current.

Finally, using the $La_2O_2CO_3:Eu^{3+}$ (5 mol %) sample prepared by $CO(NH_2)_2$ as the carbon source at different pH values for representative examples, we also investigated the effect of morphologies/sizes on their PL and CL intensities. Parts a and b of Figure 12 show a comparison of the luminescent intensities of $La_2O_2CO_3:Eu^{3+}$ (5 mol %) samples with three different morphologies/sizes under 291 nm UV light and low-voltage electron-beam excitation, respectively (here it should be mentioned that all of the experimental conditions were kept identical in order to avoid the experimental errors). It can be seen that rhombic phosphors have a higher PL/CL intensity than that of flake/flowerlike and sandwichlike spindle phosphors. It is well-known that the surface area of the materials increases with a decrease in the size. The large surface area results in a large number of defects into the phosphor crystal, which have serious impairment in the PL/CL intensity for phosphors because they provide nonradiative recombination routes for electrons and holes. In order to be as efficient as possible for the phosphors, the number of electron/hole recombinations via optically active centers must be maximized. If the surface area is greatly reduced by increasing crystallite size, the phosphor with fewer defects would show great improvement in the PL/CL intensity.[39] On the other hand, smooth and fewer exposed surfaces are also favorable to decreasing the surface area and surface defects. Although the flake/flowerlike and sandwichlike spindle samples have larger

---

(38) Feldman, C. *Phys. Rev.* **1960**, *117*, 455.

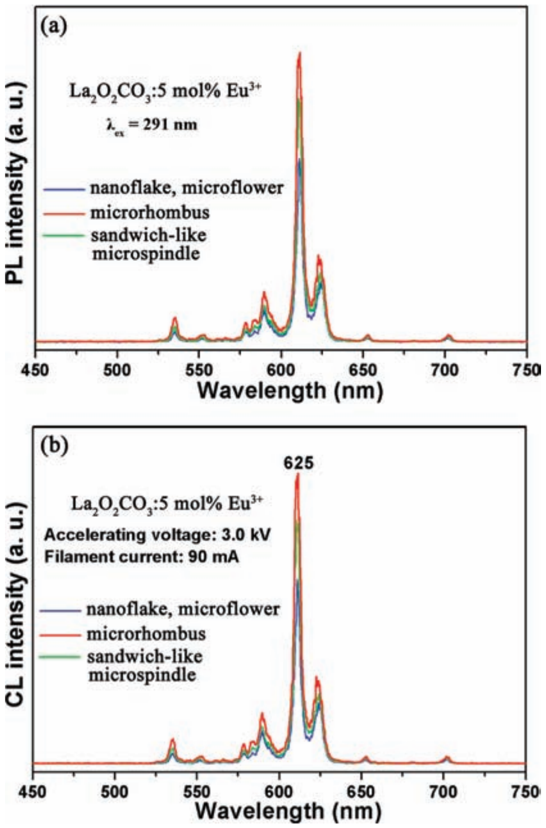

Figure 12. (a) PL and (b) CL emission spectra of the $La_2O_2CO_3$:Eu^{3+} (5 mol %) samples with three different morphologies (flake/flowerlike, rhombic, and sandwichlike spindle).

sizes than the rhombic sample, the latter has a higher luminescent intensity than the former because of the smooth and fewer exposed surfaces. Therefore, the emission intensity difference in the PL and CL results of the $La_2O_2CO_3/La_2O_3$:Ln^{3+} (Ln = Eu, Tb) products should be attributed the cooperative results of the particle size and shape, which are related to surface areas and defects. The specific surface area determined by the Brunauer–Emmett–Teller method on the flake/flowerlike, rhombic, and sandwichlike spindle $La_2O_2CO_3$:Eu^{3+} (5 mol %) samples were 7.8362, 0.0081, and 0.9918 $m^2\ g^{-1}$, respectively, which is consistent with the above conclusion. Accordingly, a large number of electrons and holes in the excited state will return to the ground state via optically radiative recombination routes for the rhombic sample. This is the reason that the PL/CL intensity of the rhombus is higher than that of flake/flowerlike and sandwichlike spindle samples.

4. Conclusion

In summary, systematic manipulation of the morphologies and architectures of $LaCO_3OH$ and $LaCO_3OH$:Ln^{3+} (Ln = Eu, Tb) nano/microcrystals on a large scale has been successfully achieved using a simple and mild solution-growth method free of any templates and catalysts. The influences of the carbon sources and pH values on the shapes of $LaCO_3OH$ and $LaCO_3OH$:Ln^{3+} (Ln = Eu, Tb) nano/microstructures have been investigated in detail. The intrinsic crystal structure of $LaCO_3OH$ and a variety of external factors account for the ultimate shape evolutions of the products. It is meaningful to investigate the morphological growth process of $LaCO_3OH$ and $LaCO_3OH$:Ln^{3+} (Ln = Eu, Tb) nano/microcrystals, which can provide important information to the fields of crystal growth and design and may be extended to the morphology-controlled creation of other rare-earth carbonate systems with complex forms. During calcination of the $LaCO_3OH$:Ln^{3+} (Ln = Eu, Tb) nano/microstructures at suitable temperatures (600 and 800 °C), we obtained the morphology-maintained $La_2O_2CO_3/La_2O_3$:Ln^{3+} (Ln = Eu, Tb). More importantly, a systematic study on the PL and CL properties of $La_2O_2CO_3/La_2O_3$:Ln^{3+} (Ln = Eu, Tb) has been explored in order to obtain multicolor-emitting phosphors. The microstructures of $La_2O_2CO_3$ and La_2O_3 and the occupations of the Eu^{3+} ions have been investigated by the excitation and site-selective emission spectra of Eu^{3+} in the two hosts. Eu^{3+} ions occupy three different sites in $La_2O_2CO_3$ by the replacement of La^{3+}, while they mainly occupy a site in the La_2O_3 matrix. In addition, there exist some clusters of Eu^{3+} ions in La_2O_3. The difference in excitation and emission spectra of Eu^{3+}- or Tb^{3+}-doped $La_2O_2CO_3$ and La_2O_3 should be attributed to the different coordination environments and symmetries of Eu^{3+} ions in $La_2O_2CO_3$ and La_2O_3 matrices. The experimental results also indicate that the optical properties of the $La_2O_2CO_3/La_2O_3$:Ln^{3+} (Ln = Eu, Tb) phosphors with different microarchitectures are strongly dependent on their morphologies and sizes.

Acknowledgment. This project is financially supported by the National Basic Research Program of China (Grants 2007CB935502 and 2010CB327704) and the National Natural Science Foundation of China (NSFC Grants 50702057, 50872131, and 20921002). The authors also thank Prof. Hyo Jin Seo and Dr. Liang Shi from Pukyong National University for their kind help in the measurement of the excitation and site-selective emission spectra of Eu^{3+} ions in the $La_2O_2CO_3/La_2O_3$:Eu^{3+} samples.

Supporting Information Available: XRD patterns of the as-prepared $LaCO_3OH$ products at pH = 7 using other carbon sources (Figure S1), FT-IR spectra of the as-synthesized $LaCO_3OH$ product (**P2**; Figure S2), parameters of the representative experiments and the morphologies and sizes of the corresponding products (Table 1), SEM images of $LaCO_3OH$ microcrystals at pH = 10 with different carbon sources: Na_2CO_3 and $(NH_4)_2CO_3$ (Figure S3), TG-DTA curves of $LaCO_3OH$ precursors (**P2**) (Figure S4), XRD patterns of $La_2O_2CO_3$ products (**M1**–**M3**) obtained by calcining $LaCO_3OH$ (**P1**–**P3**) at 600 °C for 4 h (Figure S5), XRD patterns of La_2O_3 products (**N1**–**N3**) obtained by calcining $LaCO_3OH$ (**P1**–**P3**) at 800 °C for 4 h (Figure S6), SEM images of $La_2O_2CO_3$ and La_2O_3 (**M1**, **M3**, **N1**, and **N3**) products (Figure S7), summary of the PL properties of $La_2O_2CO_3/La_2O_3$:Eu^{3+} and Tb^{3+} samples (Table 2), schematic drawing of the crystal and 3D model structures and coordination environment with O^{2-} of $La_2O_2CO_3$ and La_2O_3 (Figure S8), and $^5D_0 \rightarrow {}^7F_2$ emission decay times of Eu^{3+} ions at different crystal sites and temperatures (20–300 K) in the $La_2O_2CO_3$ and La_2O_3 hosts (Table 3). This material is available free of charge via the Internet at http://pubs.acs.org.

---

(39) (a) Yang, J.; Liu, X. M.; Li, C. X.; Quan, Z. W.; Kong, D. Y.; Lin, J. *J. Cryst. Growth* **2007**, *303*, 480. (b) Yang, J.; Li, C. X.; Cheng, Z. Y.; Zhang, X. M.; Quan, Z. W.; Zhang, C. M.; Lin, J. *J. Phys. Chem. C* **2007**, *111*, 18148.